

Frictionless dispersive hydrodynamics of Stokes flows

Michelle D. Maiden, Dalton V. Anderson, Marika E. Schubert, and Mark A. Hoefer*
Department of Applied Mathematics, University of Colorado, Boulder CO 80309, USA

Nicholas K. Lowman
(Dated: July 2, 2022)

Effectively frictionless, dispersive flow characterizes superfluids, nonlinear optical diffraction, and geophysical fluid interfaces. Dispersive shock waves (DSWs) and solitons are fundamental nonlinear excitations in these media, but DSW studies to date have been severely constrained by a loss of coherence. Here we report on a novel dispersive hydrodynamics testbed: the effectively frictionless flow of interfacial waves between two high contrast, low Reynolds' number Stokes fluids. This system enables high fidelity observations of large amplitude DSWs, found to agree quantitatively with a nonlinear wave averaging theory. We then report on observations of highly coherent phenomena including DSW backflow, the refraction or absorption of solitons by DSWs, and multi-phase DSW-DSW merger. The complex, coherent, nonlinear mixing of DSWs and solitons observed here are universal features of dissipationless, dispersive hydrodynamic flows.

The behavior of a fluid-like, dispersive medium that exhibits negligible dissipation is spectacularly realized during the process of wave breaking that generates coherent nonlinear wavetrains called dispersive shock waves (DSWs). A DSW is an expanding, oscillatory train of amplitude-ordered nonlinear waves composed of a large amplitude solitonic wave at one end attached to a monotonically decreasing wave envelope that terminates with a packet of small amplitude dispersive waves (see Fig. 1). Thus, DSWs coherently encapsulate the range of fundamental and universal features of nonlinear wave systems. More broadly, DSWs fall into the category of dispersive hydrodynamics of superfluid-like media where dissipation has negligible impact.

Shock waves and solitons are ubiquitous excitations in dispersive hydrodynamics, having been observed in many environments including quantum systems (ultra-cold atoms [1–7], semiconductor cavities [8], electron beams [9]), nonlinear optics [10–17], geophysical fluids [18–23], and cold plasma [24, 25]. However, all DSW studies to date have been severely constrained by expensive laboratory setups [1–7, 9], difficulties in capturing dynamical information [4, 11, 20], complex physical modeling [7, 20, 21], or a loss of coherence due to multi-dimensional instabilities [1, 4, 7, 8] or dissipation [9, 23, 25]. Here we report on a novel dispersive hydrodynamics testbed that circumvents all of these difficulties: the effective superflow of interfacial waves between two high viscosity contrast, low Reynolds number Stokes fluids, previously utilized as a model of magma migration [26–28]. This system enables high fidelity studies of large amplitude DSWs, which are found to agree quantitatively with nonlinear wave averaging or Whitham theory [29–32]. We then report the first experimental observations of highly coherent phenomena including DSW backflow, the refraction or absorption of solitons interacting with DSWs, and multi-phase DSW-DSW merger. In addition to its fundamental interest, the nonlinear mixing of mi-

croscopic scale solitons and mesoscopic scale DSWs could play a major role in the initiation of decoherence and a macroscopic-scale, one-dimensional, integrable turbulent state [33] that has recently been observed in optical fibers [34] and surface ocean waves [35].

In our experiment, the vertical evolution of the interface between an intrusive, buoyant, viscous liquid conduit surrounded by an exterior, miscible, much more viscous fluid exhibits wave breaking, dispersion, and no measurable dissipation [36, 37], thus the *fluid interface* can be viewed as a dispersive hydrodynamic medium. A fluid conduit is established by continuously injecting the intrusive fluid from below through a nozzle. Interfacial dynamics are excited by modulating the injection rate [38]. Figure 1(a) displays the emergence of a DSW from interfacial self-steepening due to the competition between buoyancy and interfacial stresses resulting in dispersion that preserves mass conservation as explained below. By extracting the spatial variation of the conduit cross-sectional area a , normalized by the constant downstream conduit area, from a one frame per second image sequence, we display in Fig. 1(b) the full spatio-temporal dynamics as a contour plot [38]. A carefully prescribed injection protocol [38] enables delayed breaking far from the injection site, allowing for the isolated creation and long-time propagation of a “pure” DSW connecting two uniform, distinct conduit areas. Here we have physically realized the Gurevich-Pitaevskii-Riemann problem [30], a standard textbook problem for the study of shock waves that has been inaccessible in other dispersive hydrodynamic systems. Similar excitations in the conduit system were previously interpreted as periodic wave trains modeling mantle magma transport [27]. As we now demonstrate, the interfacial dynamics observed here exhibit a soliton leading edge propagating with the nonlinear phase velocity and a harmonic wave trailing edge moving with the linear group velocity, a striking realization of the double characteristic splitting from linear wave theory [29].

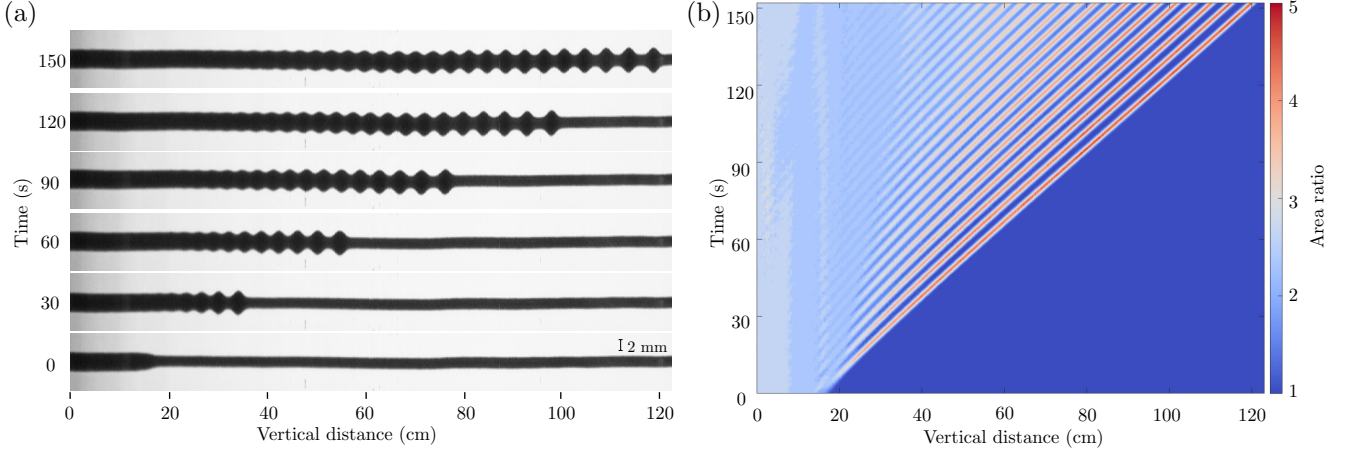


FIG. 1: Interfacial wavebreaking of two Stokes fluids causing the spontaneous emergence of coherent oscillations, a DSW. The leading, downstream edge is a large amplitude soliton whose phase speed is tied to the upstream conduit area. The trailing, upstream edge is a small amplitude wave packet moving at the group velocity whose wavenumber is tied to the downstream conduit area. (a) 90° clockwise rotated, time-lapse digital images (aspect ratio 10:1). (b) Space-time contour plot of the conduit cross-sectional area from (a). Nominal experimental parameters: $\Delta\rho = 0.0928 \text{ g/cm}^3$, $\mu_i = 91.7 \text{ cP}$, $\epsilon = 0.030$, downstream flow rate $Q_0 = 0.50 \text{ mL/min}$, and $a_- = 2.5$.

The long wavelength approximation of the fluid dynamics is the conduit equation [27, 37]

$$a_t + (a^2)_z - (a^2 (a^{-1} a_t)_z)_z = 0. \quad (1)$$

Here, subscripts denote partial derivatives, $a(z, t)$ is the nondimensional cross-sectional area of the conduit as a function of the vertical coordinate z and time t . Both the experimental conduit system and equation (1) exhibit the essential features of frictionless, dispersive hydrodynamics: nonlinear self-steepening (second term) due to buoyant advection of the intrusive fluid, dispersion (third term) from the exterior fluid's viscous resistance to motion, and no dissipation due to the combination of intrusive fluid mass conservation and negligible mass diffusion [38]. The analogy to frictionless flow corresponds to the *interfacial* dynamics, not the momentum diffusion dominated dynamics of the bulk. The conduit equation (1) is nondimensionalised according to cross-sectional area, vertical distance, and time in units of $A_0 = \pi R_0^2$, $L_0 = R_0/\sqrt{8\epsilon}$, and $T_0 = \mu_i/L_0 g \Delta\rho\epsilon$, respectively, where R_0 is the downstream conduit radius, $\epsilon = \mu_i/\mu_e$ is the viscosity ratio of the intrusive to exterior liquids, $\Delta\rho = \rho_e - \rho_i$ is the density difference, and g is gravity acceleration. Initially proposed as a simplified model for the vertical ascent of magma along narrow, viscously deformable dikes and principally used to study solitons [27, 36, 39, 40], the conduit equation (1) has since been derived systematically from the full set of coupled Navier-Stokes fluid equations using a perturbative procedure with the viscosity ratio as the small parameter [37]. The conduit equation (1) was theoretically shown to be valid for long times and large amplitudes under modest physical assumptions on the basin geometry, background

velocities, fluid compositions, weak mass to momentum diffusion, and characteristic aspect ratio. The efficacy of this model has been experimentally verified in the case of solitons [36, 39, 40].

The study of DSWs involves a nonlinear wave modulation theory, commonly referred to as Whitham theory [29], which treats a DSW as an adiabatically modulated periodic wave [30]. Recent developments [31] enable the analytical determination of key DSW physical features (leading soliton amplitude and leading/trailing speeds) under fairly general conditions. For the jump in downstream to upstream area ratio a_- , Whitham theory applied to the conduit equation (1) predicts relatively simple expressions for the DSW leading s_+ and trailing s_- edge speeds [32]

$$s_+ = \sqrt{1 + 8a_-} - 1, \quad s_- = 3 + 3a_- - 3\sqrt{a_-(8 + a_-)}, \quad (2)$$

in units of the characteristic speed $U_0 = L_0/T_0$. The leading edge corresponds to an isolated soliton where the modulated periodic wave exhibits a zero wavenumber. The soliton amplitude a_s is implicitly determined from the soliton dispersion relation [36] $s_+ = [a_s^2(2\ln a_s - 1) + 1]/(a_s - 1)^2$. At the trailing edge, the modulated wave limits to zero amplitude, corresponding to harmonic waves propagating with the group velocity $s_- = \omega'(k_-)$, where $\omega(k) = 2a_-k/(1 + a_-k^2)$ is the linear dispersion relation of eq. (1) on a background a_- and $k_-^2 = (a_- - 4 + \sqrt{a_-(8 + a_-)})/(4a_-)$ is the distinguished wavenumber determined from modulation theory [32]. In Fig. 2, we compare the leading edge amplitude and speed predictions with experiment, demonstrating quantitative agreement for a range of jump values a_- . The analyti-

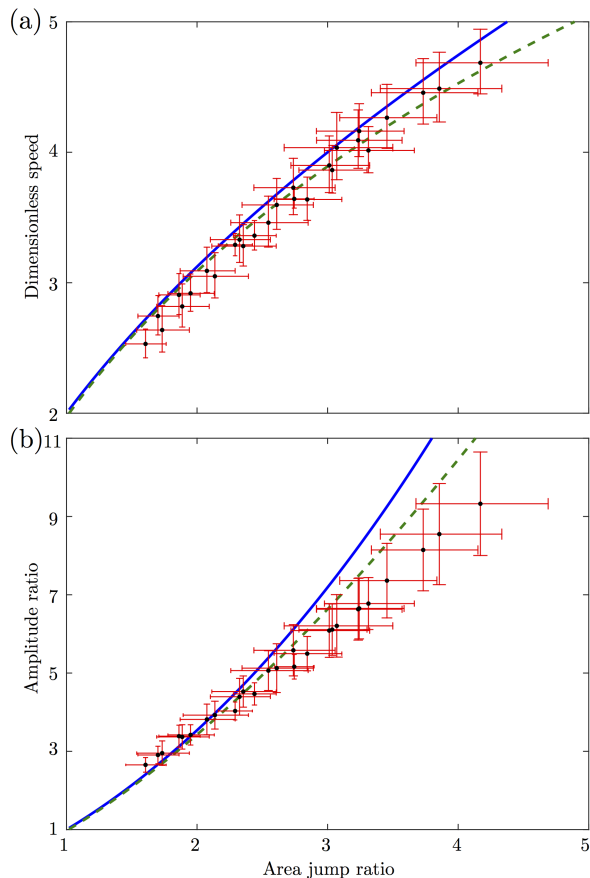


FIG. 2: Observations (circles), Whitham modulation theory (solid), and numerical simulation of the conduit equation (dashed) for (a) DSW leading edge speeds s_+ and (b) DSW leading amplitude versus downstream area ratio a_- . Nominal experimental parameters: $\Delta\rho = 0.1305$ g/cm³, $\mu_i = 80.4$ cP (measured), $\mu_i = 104$ cP (fitted), $\epsilon = 0.0024$. See [38] for fitting procedure.

cal theory (Whitham theory) is known to break down at large amplitudes [32] so we also include direct determination of the speed and amplitude from numerical simulation of eq. (1), demonstrating even better agreement. The deviation between experiment and theory at large jump values is consistent with previous measurements of solitons, where the soliton dispersion relation was found to underpredict observed speeds at large amplitudes [36]. See [38].

Our experimental setup allows us to investigate exotic, coherent effects predicted by eq. (1) for the first time. For example, backflow is a feature of dispersive hydrodynamic systems whereby a portion of the DSW envelope propagates upstream. This feature occurs here when the group velocity of the trailing edge wave packet is negative. From the expression for s_- , we predict the onset of backflow when a_- exceeds $8/3$. In Fig. 3, we utilize our injection protocol to report the observation of this phenomenon in the viscous conduit setting [38].

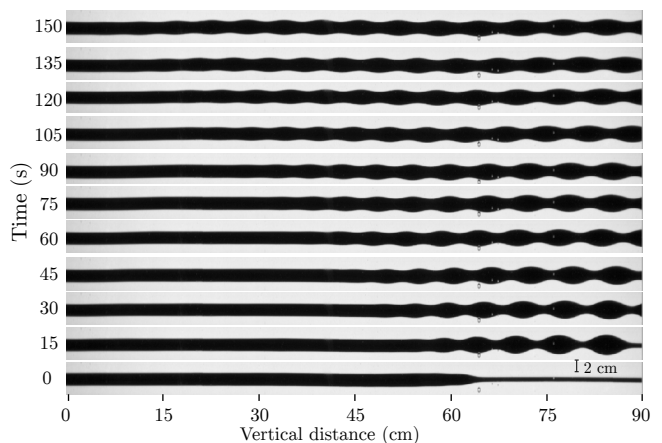


FIG. 3: Time-lapse images (aspect ratio 1:1) of large amplitude wavebreaking leading to upstream propagation of the DSW trailing edge envelope: DSW backflow. Nominal experimental parameters: $\Delta\rho = 0.0983$ g/cm³, $\mu_i = 93.5$ cP, $\epsilon = 0.029$, $a_- = 4$, and $Q_0 = 0.50$ mL/min.

Waves with strictly positive phase velocity are continually generated at the trailing edge but the envelope group velocity is negative. This behavior is reminiscent of slow light in optical systems where manipulation of the propagation medium's dispersion properties enables the effective slowing down or stopping of light [41]. We estimate the crossover to backflow for the experiments reported in Fig. 2 at $a_- \approx 3$. We expect a slightly larger crossover than theory ($8/3$) due to sub-imaging-resolution of small amplitude waves.

The ease with which DSWs and solitons can be created in this viscous liquid conduit system enables the investigation of novel coherent, nonlinear wave interactions [38]. In Fig. 4, we report soliton-DSW and DSW-DSW interactions. Figures 4(a,b) depict a DSW followed by a soliton. Because solitons propagate with a nonlinear phase velocity larger than the linear wave phase and group velocities [36], the soliton eventually overtakes the DSW trailing edge. The soliton-DSW interaction results in a sequence of phase shifts owing to the general interpretation of a DSW as a modulated soliton train. The soliton emerges from the interaction with a significantly increased amplitude and decreased speed due to the smaller downstream conduit upon which it is propagating. The initial and final slopes of soliton propagation in Fig. 4(b) demonstrate that the soliton has been refracted by the DSW. Meanwhile, the DSW experiences a subtle phase shift and is otherwise unchanged.

The opposite problem of a soliton being overtaken by a DSW is displayed in Fig. 4(c). After multiple phase shifts during interaction, the soliton is slowed down and effectively absorbed within the interior of the DSW, while the DSW is apparently unchanged except for a phase shift in its leading portion. Such behavior is consistent with

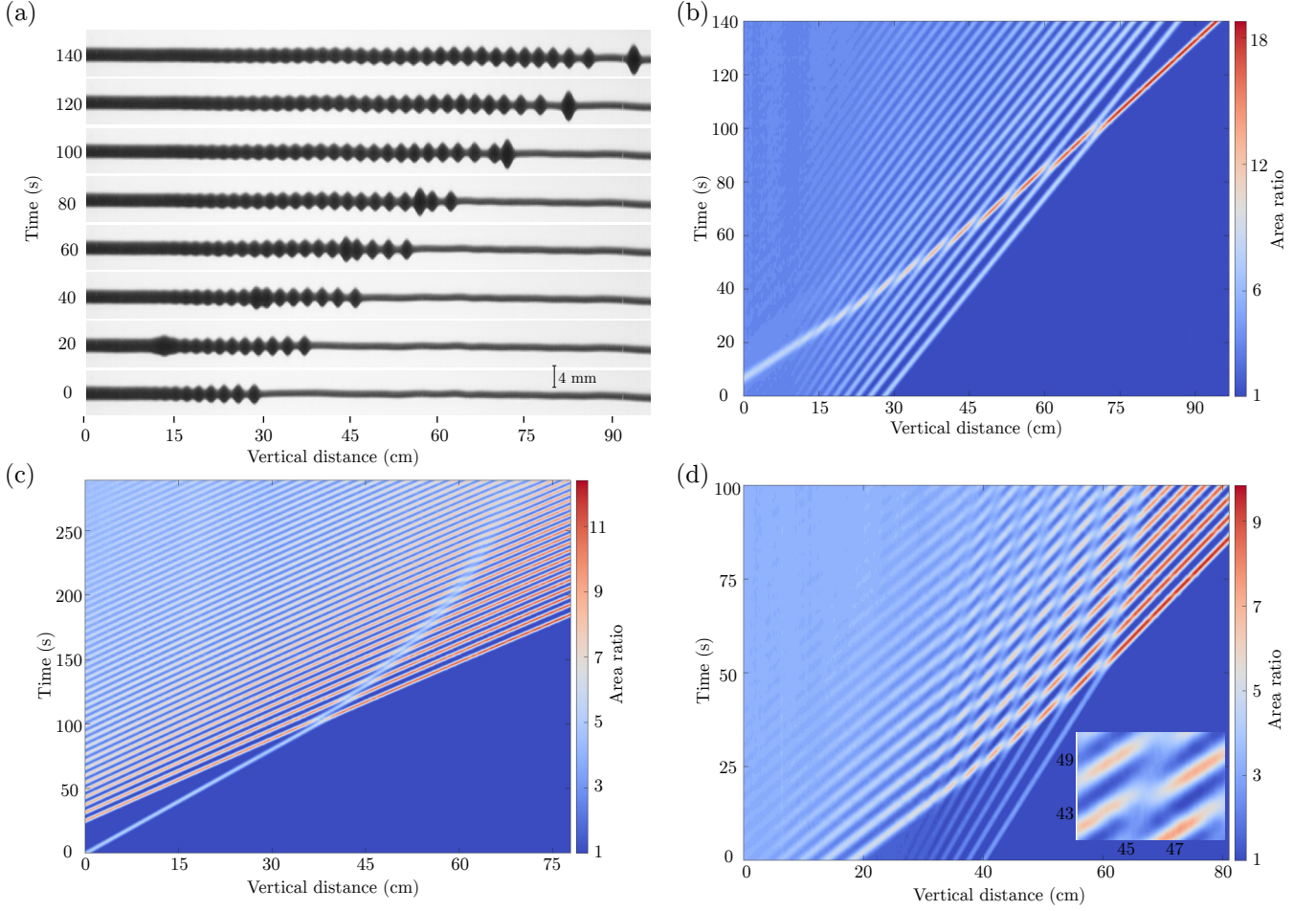


FIG. 4: Interactions of solitons and DSWs. Time-lapse images with aspect ratio 10:1 (a) and space-time contour (b) of DSW-soliton interaction revealing soliton refraction by a DSW with $a_- = 3$. (c) Space-time contour of the absorption of a soliton by a DSW with $a_- = 3.5$. (d) DSW-DSW interaction and merger causing multiphase mixing (inset) and the refraction of the trailing DSW by the leading DSW with $a_1 = 2.5$, $a_2 = 5$. Nominal experimental parameters: $\Delta\rho = 0.0971$ g/cm³, $\mu_i = 99.1$ cP, $\epsilon = 0.029$, $Q_0 = 0.2$ mL/min.

the interpretation of a DSW as a modulated wavetrain with small amplitude trailing waves that will always move slower than a finite amplitude soliton.

Finally, Fig. 4(d) reveals the interaction of two DSWs. The interaction region results in a series of phase shifts due to soliton-soliton interactions that form a quasiperiodic or two-phase wavetrain as shown in the inset. This nonlinear mixing eventually subsides, leaving a single DSW representing the merger of the original two. The trailing DSW has effectively been refracted by the leading DSW.

We can interpret the soliton and DSW refraction as follows. First, consider the overtaking interaction of two DSWs. Denote the midstream and upstream conduit areas $a_1 < a_2$ relative to the downstream area $a_0 = 1$. Equation (2) implies the leading edge speeds of the first and second DSWs are $s_1 = \sqrt{1 + 8a_1} - 1$, $s_2 = a_1(\sqrt{9 + 8(a_2 - 1)/a_1} - 1)$. Motivated by previous

DSW interaction studies [42–44], we assume merger of the two DSWs and thus obtain the leading edge speed of the merged DSW $s_m = 4\sqrt{\frac{1}{2}(a_1 + a_2) - 1} - 1$ connecting conduit areas a_0 to a_2 . One can verify the interleaving property $s_1 < s_m < s_2$, demonstrating the refraction (slowing down) of the second DSW. If we treat the isolated soliton as the leading edge of a DSW, then we obtain the same result for soliton-DSW refraction.

Viscous liquid conduits are a model system for the coherent dynamics of one-dimensional superfluids with mesoscopic-scale dispersive shock waves and microscopic-scale solitons as fundamental nonlinear excitations. Interaction of DSWs and solitons suggest that soliton refraction, absorption, multi-phase dynamics, and DSW merging are general, universal features of superfluidic dispersive hydrodynamics. The viscous liquid conduit system is a new environment in which to investigate complex, coherent dispersive hydrodynamics, inaccessible in

other superfluids or superfluid-like media.

M.A.H. is grateful to Marc Spiegelman for bringing the viscous liquid conduit system to his attention and to Genady El for his support on this work. We thank Weiliang Sun for help with measuring the mass diffusion properties of fluids used in this work. This work was partially supported by NSF CAREER DMS-1255422 (M.A.H., D.V.A.), NSF GRFP (M.D.M., N.K.L.), and NSF EXTREEMS-QED DMS-1407340 (D.V.A., M.E.S.).

* Electronic address: hoefer@colorado.edu

- [1] Z. Dutton *et al.*, Science **293**, 663 (2001).
- [2] T. P. Simula, *et al.*, Phys. Rev. Lett. **94**, 080404 (2005).
- [3] M. A. Hoefer, *et al.*, Phys. Rev. A **74**, 023623 (2006).
- [4] J. J. Chang, P. Engels, and M. A. Hoefer, Phys. Rev. Lett. **101**, 170404 (2008).
- [5] M. A. Hoefer, P. Engels, and J. Chang, Physica D **238**, 1311 (2009).
- [6] R. Meppelink, *et al.*, Phys. Rev. A **80**, 043606 (2009).
- [7] J. A. Joseph, *et al.*, Phys. Rev. Lett. **106**, 150401 (2011).
- [8] A. Amo, *et al.*, Science **332**, 1167 (2011).
- [9] Y. C. Mo, *et al.*, Phys. Rev. Lett. **110**, 084802 (2013).
- [10] J. E. Rothenberg and D. Grischkowsky, Phys. Rev. Lett. **62**, 531 (1989).
- [11] W. Wan, S. Jia, and J. W. Fleischer, Nat. Phys. **3**, 46 (2007).
- [12] S. Jia, W. Wan, and J. W. Fleischer, Phys. Rev. Lett. **99**, 223901 (2007).
- [13] C. Barsi, *et al.*, Opt. Lett. **32**, 2930 (2007).
- [14] C. Conti, *et al.*, Phys. Rev. Lett. **102**, 083902 (2009).
- [15] C. Barsi, *et al.*, in *Nonlinear Photonics and Novel Optical Phenomena*, edited by Z. Chen and R. Morandotti (Springer Berlin, 2012), pp. 231–257.
- [16] N. Ghofraniha, *et al.*, Opt. Lett. **37**, 2325 (2012).
- [17] J. Fatome, *et al.*, Phys. Rev. X **4** (2014).
- [18] J. L. Hammack and H. Segur, J. Fluid Mech. **84**, 337 (1978).
- [19] D. Farmer and L. Armi, Science **283**, 188 (1999).
- [20] A. Porter and N. F. Smyth, J. Fluid Mech. **454**, 1 (2002).
- [21] C. R. Jackson, Tech. Rep., Global Ocean Associates (2004), URL http://www.internalwaveatlas.com/Atlas2_index.html.
- [22] A. Scotti, *et al.*, J. Geophys. Res. **113** (2008).
- [23] H. Chanson, Eur. J. Mech. B **28**, 191 (2009).
- [24] R. J. Taylor, D. R. Baker, and H. Ikezi, Phys. Rev. Lett. **24**, 206 (1970).
- [25] M. Q. Tran, *et al.*, Plasma Phys. **19**, 381 (1977).
- [26] D. R. Scott and D. J. Stevenson, Geophys. Res. Lett. **11**, 1161 (1984).
- [27] D. R. Scott, D. J. Stevenson, and J. A. Whitehead, Nature **319**, 759 (1986).
- [28] J. A. Whitehead and K. R. Helfrich, Nature **336**, 59 (1988).
- [29] G. B. Whitham, *Linear and Nonlinear Waves* (Wiley, New York, 1974).
- [30] A. V. Gurevich and L. P. Pitaevskii, Sov. Phys. JETP **38**, 291 (1974).
- [31] G. A. El, Chaos **15**, 037103 (2005).
- [32] N. K. Lowman and M. A. Hoefer, J. Fluid Mech. **718**, 524–557 (2013).
- [33] G. A. El and A. M. Kamchatnov, Phys. Rev. Lett. **95**, 204101 (2005).
- [34] S. Randoux, *et al.*, Phys. Rev. Lett. **113**, 113902 (2014).
- [35] A. Costa, *et al.*, Phys. Rev. Lett. **113**, 108501 (2014).
- [36] P. Olson and U. Christensen, J. Geophys. Res. **91**, 6367 (1986).
- [37] N. K. Lowman and M. A. Hoefer, Phys. Rev. E **88**, 023016 (2013).
- [38] See Supplemental Material at [URL] for additional experimental details and videos corresponding to each Figure.
- [39] K. R. Helfrich and J. A. Whitehead, Geophys. Astro. Fluid Dyn. **51**, 35 (1990).
- [40] N. Lowman, M. Hoefer, and G. El, J. Fluid Mech. **750**, 372 (2014).
- [41] L. V. Hau, *et al.*, Nature **397**, 594 (1999).
- [42] M. A. Hoefer and M. J. Ablowitz, Physica D **236**, 44 (2007).
- [43] M. J. Ablowitz, D. E. Baldwin, and M. A. Hoefer, Phys. Rev. E **80**, 016603 (2009).
- [44] M. J. Ablowitz and D. E. Baldwin, Phys. Rev. E **87**, 022906 (2013).

Supplemental materials for “Frictionless dispersive hydrodynamics of Stokes flows”

Michelle D. Maiden, Dalton V. Anderson, Marika E. Schubert, and Mark A. Hoefer
Department of Applied Mathematics, University of Colorado, Boulder CO 80309, USA
 Nicholas K. Lowman
 (Dated: July 2, 2022)

In this supplemental material, additional experimental details are provided.

POISEUILLE FLOW RELATION

The conduit experimental data are obtained by injecting through a 0.22 cm inner diameter nozzle an approximately 7:2:1 mixture of corn syrup (Karo brand light), water, and black food coloring (Regal brand) into the bottom of a 2 m tall acrylic, 25.8 cm² square column filled with corn syrup (3:2 mixture of Golden Barrel brand 42 dextrose equivalent and Karo brand light for data of Figure 2, pure Karo brand light for Figures 1, 3, 4). The fluid temperature near the top of the fluid column was measured to be 22.2 ± 0.7 deg C across all experimental trials. A computer controlled piston pump (Global FIA milliGat LF pump with MicroLynx controller) was used to inject fluid through a room temperature water bath followed by the nozzle. See Fig. S1 for an experimental schematic. When the injected fluid reaches the top of the fluid column, it pools on top of the external fluid and very slowly begins to diffuse downward. We periodically removed the pooling fluid with a syringe. Steady injection results in a vertically uniform liquid filled pipe or conduit conforming to Poiseuille flow [S1, S2]. We allowed the conduit to stabilize (straighten) by steady injection over a period of 36 hours for the data in Fig. 2 and 15 hours for the other data.

The quantitative data in Fig. 2 exhibits typical conduit diameters of one to four millimetres and Reynolds numbers in the range $Re = \rho_i U_0 L_0 / \mu_i \in (0.06, 2.6)$, where ρ_i is the intrusive fluid density. We can set the conduit diameter D via the volumetric flow rate Q according to a Hagan-Poiseuille relation [S2] $D = \alpha Q^{1/4} = (2^7 \mu_i Q)^{1/4} / (\pi g \Delta \rho)^{1/4}$. Digital images of the conduit are processed to extract the conduit diameter. The conduit edges are determined from local extrema of the differentiated grayscale intensity image using centred differences in the direction normal to the conduit interface. We confirm the Poiseuille flow relation $D = \alpha Q^{1/4}$ for the trials of Fig. 2 approximately 6 cm above the fluid injection site with no fitting parameters (Fig. S2). In Fig. S3, we show the fit of the Poiseuille flow relation to the same conduit, imaged approximately 120 cm above the injection site. The difference between the externally measured viscosity $\mu_i = 80.4$ cP and the value $\mu_i = 104$ cP from a fit to the Poiseuille flow relation can be explained by the non-Newtonian, thixotropic (shear thinning) properties of corn syrup. At the injection site, the diluted corn syrup experiences heightened shearing, similar to our rotational viscometer measurements (Brookfield DV-I prime viscometer). Further up the fluid column, there is less shearing so the fluid increases in viscosity and leads to a dilation of the conduit. The conduit consistently has a measured diameter in the upper fluid column that is 7% larger than its value near the injection site as shown in Fig. S4. The results in Fig. 2 of the main text use the measured value of $\Delta \rho$ and the fitted value $\mu_i = 104$ cP.

DSW AND SOLITON INJECTION PROTOCOL.

By adiabatically changing Q , we introduce perturbations to the conduit that subsequently propagate along the interface, allowing for the generation of conduit solitons [S3–S6] and DSWs. The injection rate profile for solitons is generated by computing a conduit solitary wave solution $a_{\text{soliton}}(z - ct - z_0)$ with speed c and initial center z_0 to eq. (1). This profile is converted to the dimensional diameter $D_{\text{soliton}} = 2\sqrt{a_{\text{soliton}} A_0 / \pi}$ and then the volumetric flow rate profile $Q_{\text{soliton}} = (D_{\text{soliton}} / \alpha)^4$, evaluated at the injection site.

The volumetric flow rate profile Q_{DSW} that we use to create DSWs is determined as follows. We initialize the dispersionless conduit equation $a_t + (a^2)_z = 0$ with a step in conduit area from a_- to 1, left to right, at a desired distance from the nozzle $z = z_b$. Evolving this initial value problem backward in time results in a non-centered rarefaction wave that can be related to the volumetric flow rate profile via

$$Q_{\text{DSW}}(\tau) = Q_0 \begin{cases} 1 & t \leq 0 \\ (1 - 2\tau U_0 / Z_b)^{-2} & 0 < \tau U_0 / Z_b < (a_- - 1) / 2a_- \\ a_-^2 & \text{else} \end{cases},$$

where Q_0 is the downstream flow rate, τ is the dimensional time, and $Z_b = L_0 z_b$ is the dimensional breaking distance from the injection site. We find that this provides adequate control over the breaking location.

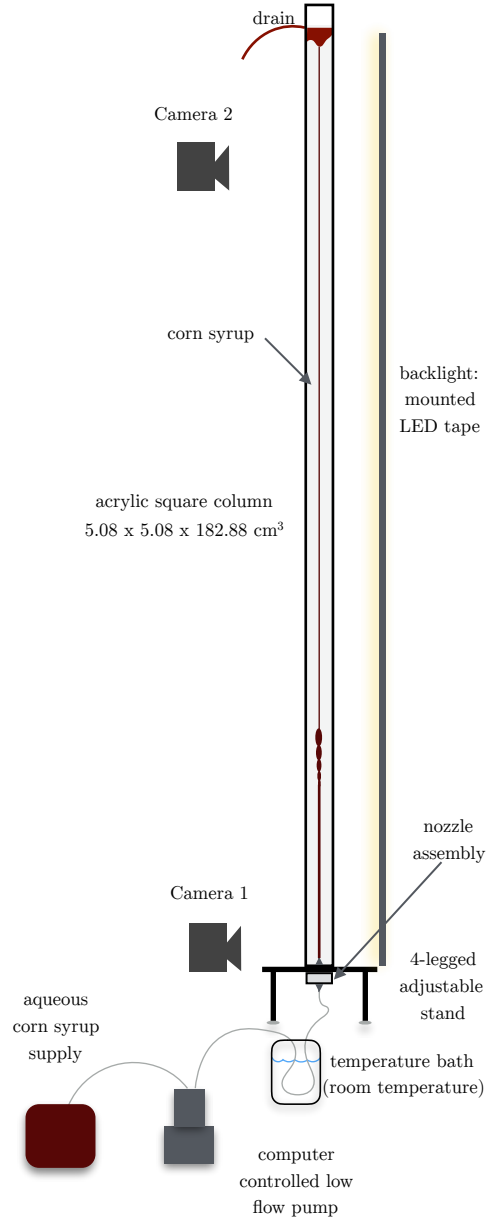


FIG. S1: Schematic of the conduit experimental apparatus.

Each DSW trial in Fig. 2 was initiated after a sufficient waiting period, typically 5 minutes, to allow the previous trial's conduit diameter to stabilize to the expected steady value. The downstream flow rates utilized for the data in Fig. 2 were nominally $Q_0 \in \{0.25, 0.35, 0.5\}$ mL/min. Three digital SLR cameras were utilized, two Canon EOS 70D cameras outfitted with Tamron macro lenses positioned just above the injection site (camera one) and at approximately 120 cm above the injection site (camera two). The third camera (Canon EOS Rebel T5i), outfitted with a zoom lens, was used to image the entire vertical length of 120 cm from the injection site. The fluid column was backlit with strip LED lights behind LEE LE251R white diffusion filter paper. Each DSW trial was initiated with an image of the conduit at the injection site followed by the injection protocol Q_{DSW} . The third camera was then set to image the full column every second throughout the trial. Just after the injection protocol reached the maximum rate a_-Q_0 , an image of the conduit from camera 1 was taken. Just prior to the arrival of the DSW leading edge within the viewing area of camera two, an image of the downstream conduit was taken, followed by a dozen or more images taken in rapid succession of the DSW leading edge.

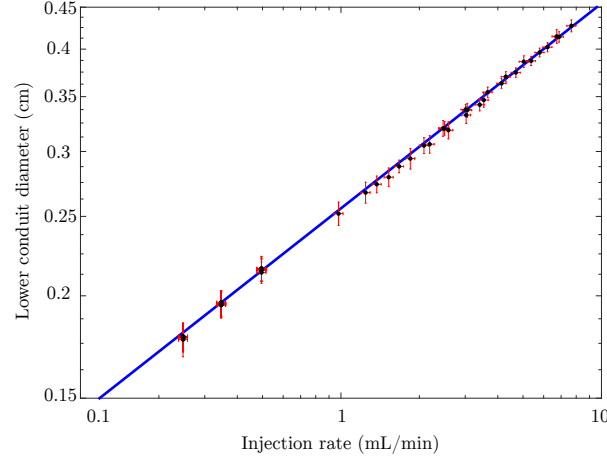


FIG. S2: Demonstration of Poiseuille flow in a steady viscous fluid conduit. Log-log plot of measured conduit diameter D near injection site versus volumetric flow rate Q (dots) and the relation $D = \alpha Q^{1/4}$ with the measured value $\alpha = 0.2557 \text{ (cm}\cdot\text{min)}^{1/4}$ (solid) corresponding to $\mu_i = 80.4 \text{ cP}$, $\Delta\rho = 0.1305 \text{ g/cm}^3$. A least squares fit gives $\alpha = 0.2548 \text{ (cm}\cdot\text{min)}^{1/4}$, which translates to the fitted viscosity $\mu_i = 79.0 \text{ cP}$, within the 2% error tolerance of our rotational viscometer.

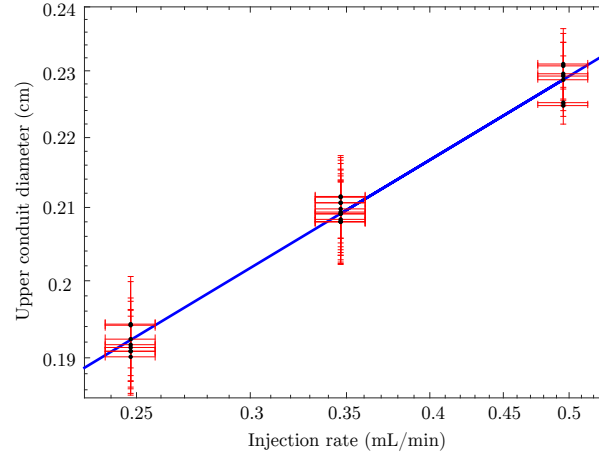


FIG. S3: Poiseuille flow fit approximately 120 cm up the fluid column. Downstream conduit diameters D extracted from digital images (dots) and a least squares fit to the Poiseuille flow relation $D = \alpha Q^{1/4}$ with $\alpha = 0.2688 \text{ (cm}\cdot\text{min)}^{1/4}$ (solid). The fit corresponds to the interior viscosity $\mu_i = 104 \text{ cP}$, an increase from its measured value $\mu_i = 80.4 \text{ cP}$. This can be explained by the shear thinning properties of corn syrup as described in Methods.

DETERMINATION OF DSW SPEED AND AMPLITUDE.

The leading edge of the DSW amplitude, normalised to the downstream area, is determined from the digital images of camera 2 without appealing to any fluid parameters. We compute the conduit edges as for the steady case, using extrema of the differentiated image intensity normal to the conduit interface. Some image and edge smoothing is performed to remove pixel noise. The number of pixels across the diameter of the leading edge DSW peak is calculated and normalized by the diameter of the downstream conduit. Squaring this quantity gives the leading edge DSW amplitude shown in Fig. 2. We calculated the leading edge DSW speed from the images of camera three toward the end of the trial. We nondimensionalise the speed by the characteristic speed $U_0 = L_0/T_0 = gA_0\Delta\rho/(8\pi\mu_i)$, where we use the measured values of the downstream flow area A_0 from camera two and $\Delta\rho$. The fitted value for μ_i is used, as described in the earlier section on Poiseuille flow.

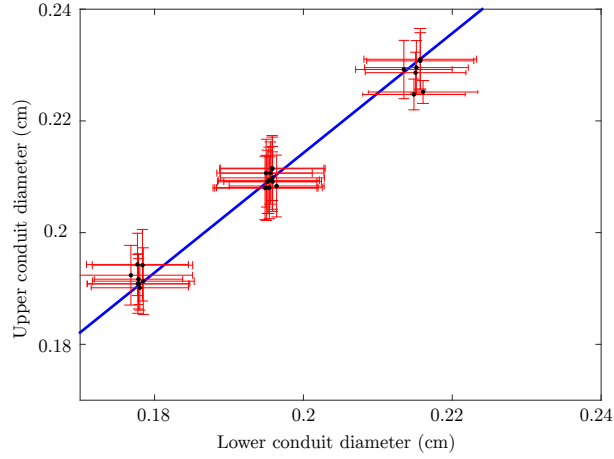


FIG. S4: Comparison of conduit diameter at different locations along the fluid column. Measurements (dots) and the linear fit $D_{\text{top}} = mD_{\text{bottom}}$ (solid) with $m = 1.07$ corresponding to a 7% increase in the conduit diameter. The lower (upper) diameter was measured approximately 6 cm (120 cm) above the injection site.

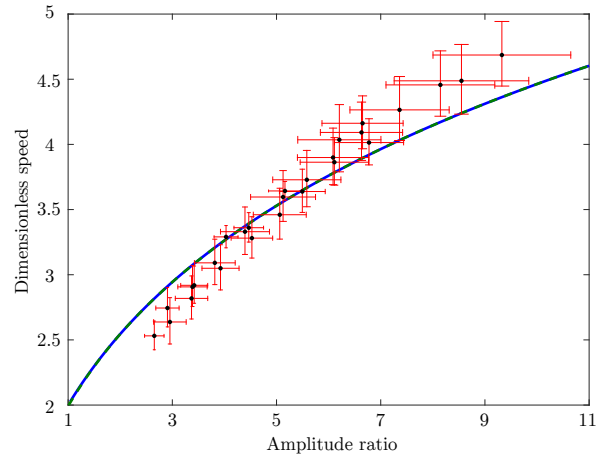


FIG. S5: DSW leading edge speed versus amplitude. The observed values (dots) and the theoretical soliton dispersion relation (solid) corresponding to Fig. 2(a,b) in the main text. The deviation at large amplitudes is consistent with previous studies of isolated solitons [S3].

MASS DIFFUSION.

The injected and external fluids are miscible so there is unavoidable mass diffusion across an interface between the two. Using a procedure similar to that described in [S7], we estimate the diffusion constant \tilde{D} between a 7:3 corn syrup, water mixture and pure corn syrup (Karo brand light) to be approximately $1.2 \times 10^{-6} \text{ cm}^2/\text{s}$. Combining this with typical flow parameters, we estimate the Péclet and Schmidt numbers for the trials of Fig. 2 to lie in the range $\text{Pe} = L_0 U_0 / \tilde{D} \in (2.1 \times 10^4, 7.9 \times 10^5)$ and $\text{Sc} = \text{Pe}/\text{Re} \approx 5.2 \times 10^5$. The advective time scale for Fig. 2 trials is in the range $T_0 \in (1.6, 5.6) \text{ s}$. We therefore estimate that mass diffusion begins to play a role after approximately 9 hours, whereas the time scale of an experimental trial is less than 10 minutes.

* Electronic address: hoefer@colorado.edu

[S1] D. R. Scott, D. J. Stevenson, and J. A. Whitehead, *Nature* **319**, 759 (1986).

[S2] J. A. Whitehead and D. S. Luther, *J. Geophys. Res.* **80**, 705 (1975).

- [S3] P. Olson and U. Christensen, *J. Geophys. Res.* **91**, 6367 (1986).
- [S4] J. A. Whitehead and K. R. Helfrich, *Nature* **336**, 59 (1988).
- [S5] K. R. Helfrich and J. A. Whitehead, *Geophys. Astro. Fluid Dyn.* **51**, 35 (1990).
- [S6] N. Lowman, M. Hoefer, and G. El, *J. Fluid Mech.* **750**, 372 (2014).
- [S7] E. Ray, P. Bunton, and J. A. Pojman, *Amer. J. Phys.* **75**, 903 (2007).